



This is a repository copy of *Application of a multi-component mean field model to the coarsening behaviour of a nickel-based superalloy*.

White Rose Research Online URL for this paper:
<http://eprints.whiterose.ac.uk/156152/>

Version: Accepted Version

Article:

Anderson, M.J. orcid.org/0000-0001-5552-4459, Rowe, A., Wells, J. et al. (1 more author) (2016) Application of a multi-component mean field model to the coarsening behaviour of a nickel-based superalloy. *Acta Materialia*, 114. pp. 80-96. ISSN 1359-6454

<https://doi.org/10.1016/j.actamat.2016.05.024>

Article available under the terms of the CC-BY-NC-ND licence
(<https://creativecommons.org/licenses/by-nc-nd/4.0/>).

Reuse

This article is distributed under the terms of the Creative Commons Attribution-NonCommercial-NoDerivs (CC BY-NC-ND) licence. This licence only allows you to download this work and share it with others as long as you credit the authors, but you can't change the article in any way or use it commercially. More information and the full terms of the licence here: <https://creativecommons.org/licenses/>

Takedown

If you consider content in White Rose Research Online to be in breach of UK law, please notify us by emailing eprints@whiterose.ac.uk including the URL of the record and the reason for the withdrawal request.



eprints@whiterose.ac.uk
<https://eprints.whiterose.ac.uk/>

Application of a multi-component mean field model to the coarsening behaviour of a nickel-based superalloy

M.J. Anderson^a, A. Rowe^b, J. Wells^{b,c}, H.C. Basoalto^a

^a*School of Metallurgy and Materials, University of Birmingham, Edgbaston, Birmingham B15 2TT, UK*

^b*RWE Npower Group plc, Windmill Hill Business Park, Whitehill Way, Swindon SN5 6PB*

^c*Currently at Siemens plc.*

Abstract

A multi-component mean field model has been applied to predict the particle evolution of the γ' particles in the nickel based superalloy IN738LC, capturing the transition from an initial multimodal particle distribution towards a unimodal distribution. Experiments have been performed to measure the coarsening behaviour during isothermal heat treatments using quantitative analysis of micrographs. The three dimensional size of the γ' particles has been approximated for use in simulation. A coupled thermodynamic/mean field modelling framework is presented and applied to describe the particle size evolution. A robust numerical implementation of the model is detailed that makes use of surrogate models to capture the thermodynamics. Different descriptions of the particle growth rate of non-dilute particle systems have been explored. A numerical investigation of the influence of scatter in chemical composition upon the particle size distribution evolution has been carried out. It is shown how the tolerance in chemical composition of a given alloy can impact particle coarsening behaviour. Such predictive capability is of interest in understanding variation in component performance and the refinement of chemical composition tolerances. It has been found that the inclusion of misfit strain within the current model formulation does not have a significant affect upon predicted long term particle coarsening behaviour. Model predictions show good agreement with experimental data. In particular, the model predicts a reduced growth rate of the mean particle size during the transition from bimodal to unimodal distributions.

Keywords: Nickel based superalloy, IN738LC, particle coarsening, mean field theory, multi-components systems

1. Introduction

Nickel based superalloys are commonly used in the energy and aerospace industry for turbine components which operate at elevated temperatures and complex mechanical loading conditions. These alloys are precipitation strengthened through the presence of the γ' intermetallic phase. The stability of the γ' particles during thermal exposure has a significant impact upon mechanical properties and thus component performance [1]. The Nickel based superalloys used in turbine applications are often heat treated to obtain a multi-modal distribution of γ' , which are characterised by the mean size of each population. With exposure to elevated temperature, the γ' particles coarsen towards a unimodal distribution of particles, as observed in the superalloy Nimonic 115 [2]. The ability to predict the evolution of the size and volume fraction of γ' is needed in the development of location specific property prediction capabilities that explicitly link the particle dispersion to the constitutive response of the material [3].

The evolution of the γ' particle size distribution is influenced by a number of diffusion related mechanisms, which include growth, coarsening, morphology changes and the coalescence of particles. In the scientific literature a number of theoretical and numerical frameworks have been presented to model such behaviour with varying levels of details. Phase field and sharp interface models are effective in capturing the change in particle morphology, overlapping diffusion fields, and the impact of the elastic misfit of the particles [4]. A challenge of applying such methods to predict the particle kinetics during long thermal exposures is dealing with the change in representative volume size that captures a statistically relevant number of precipitates.

A less computationally expensive method for predicting the transition of a multi-modal particle size distribution towards a unimodal dispersion is a mean

field theory description of particle growth [5]. Greenwood [6], Lifshitz and Slyozov [7] and Wagner [8] (LSW) derived the first complete mean field description of particle coarsening in dilute binary alloy systems. Important findings of these models include the predicted behaviour that any given distribution of particles coarsen towards an asymptotic shape and that the predicted coarsening rate of the mean particle size reaches a value proportionate to $time^{1/3}$.

The theory proposed by LSW describes the coarsening kinetics of a dilute dispersion of particles in a binary alloy and over the last two decades or so, progress has been made in the extension of the approach to model multi-component alloys. The simplest approach is to treat a multi-component alloy as a pseudo-binary system, considering the diffusion of the particle forming species. Such an approach was applied by Coakley *et al.* [2] to simulate the coarsening kinetics of Nimonic 115. A CALPHAD approach [9] allows for calculation of the chemical composition of the particle phase and the Gibbs free energy of the system. A mobility database can allow for the calculation of the effective diffusivity of the particle interface, considering the local chemical composition. Kuehmann and Voorhees [10] developed a model descriptive of ternary alloys which has been successfully implemented by Mao *et al.* [11] to a ternary Nickel based superalloy. Jou *et al.* [12] developed a generic approach to extending the Kuehmann and Voorhees model to multiple alloying elements. Collins and Stone [13] have applied a similar model to optimise the particle dispersion within the Nickel based superalloy RR1000. The derivation of the multi-component particle growth rate has been further refined by Phillipe and Voorhees [14]. Svoboda *et al.* [15] have also developed a multi-component model, which Radis *et al.* [16] have applied to the Nickel based superalloy Udimet 720. This model has been implemented in this work and is referred to as the Svoboda-Fischer-Fratzl-Kozeschnik (SFFK) model.

The mean field approach of LSW describes a dilute system of particles where the diffusion field and elastic distortion of neighbouring particles do not interact. Baldan [17] reviewed several mean field approaches to describing the impact of non-zero fraction particle systems and found that the descriptions qualita-

tively captured the relationship between volume fraction and coarsening kinetics however lacked quantitative accuracy. A recent contribution by Svoboda and Fischer [18] builds upon the work of Voorhees and Glicksman [19] and Marqusee and Ross [20] that accounts for competitive growth between particles. A complimentary approach to extend LSW mean field theory to include particle coalescence has been derived by Davies *et al.* [21]. The implication of particle coalescence is to be discussed in a separate paper. The treatment of high volume fraction particle systems using a LSW mean field approach remains an active field of research [22].

The objective of this paper is to further develop the understanding and ability to predict the evolution of multi-modal particle systems, linking chemical composition to particle coarsening behaviour. This paper focuses upon the coarsening kinetics of the intragranular γ' particles in the Inconel 738LC. This builds upon the work of Coakley *et al.* [2] on Nimonic 115 through the methods used to approximate the 3D size of the particles and the application of a multi-component description of the alloy behaviour. Different approaches to the description of high volume fraction particle systems have been assessed. To support these model developments, isothermal heat treatments have been applied to coupons of the alloy obtained in the as-heat treated condition, capturing behaviour relevant to the operating temperature of turbine engine components. This work is part of an integrated computational materials engineering (ICME) work programme designed to develop location specific property prediction models, allowing for the optimisation of component performance and heat treatment.

The paper is divided in the following sections. Section 2 gives details regarding the experimental conditions, the observed microstructure and the results from quantitative microstructural analysis. Section 3 presents the mean field model and normalised formulation. The model parameters and numerical methods used to perform the calculations are provided in an implementation section. The comparison of predicted and measured behaviour are presented in a results and discussion section.

Table 1: Chemical composition of IN738LC (wt.%)

	Al	B	C	Co	Cr	Mo
Lower	3.2	0.007	0.09	8	15.7	0.6
Nominal	3.4	0.01	0.11	8.5	16	1.75
Upper	3.7	0.012	0.13	9	16.3	2
	Nb	Ni	Ta	Ti	W	Zr
Lower	0.6		1.5	3.2	2.4	0.03
Nominal	0.9	bal	1.75	3.4	2.6	0.05
Upper	1.1		2	3.7	2.8	0.08

2. Experimental

The chemical composition of IN738LC is given in table 2. Coupons of conventionally cast heat treated IN738LC have been isothermally aged for a maximum of 20,000 hours at temperatures of 850°C and 900°C. Coarsening of the γ' dispersion was observed after thermal exposure for 1000, 2000, 5000, 10000 and 20000 hours for both temperatures. The samples were mechanically polished and electrochemically etched in solution of 2% phosphoric acid in water.

The characterisation procedure is similar to that described by Payton *et al.* [23], capturing the precipitates using FEG-SEM with the back-scattered imaging method. The as-received microstructure is shown in figure 1. Upon further magnification (1(b)) the γ' dispersion appears to be tri-modal. The largest population of particles within the grains are cuboidal in morphology. Some of these particles have a serrated surface. These protrusions may be caused by instabilities on interfaces during growth or through coalescence with smaller particles. As the growth of such protrusions would increase interfacial energy significantly, it is likely that these are caused through coalescence. The secondary particles have a globular form, with some particles appearing to be an amalgamation of several smaller particles. The third population are fine spherical particles which quickly dissolve at the high temperatures of interest.

Micrographs of the coarsened structures are shown in Figures 2 and 3 for

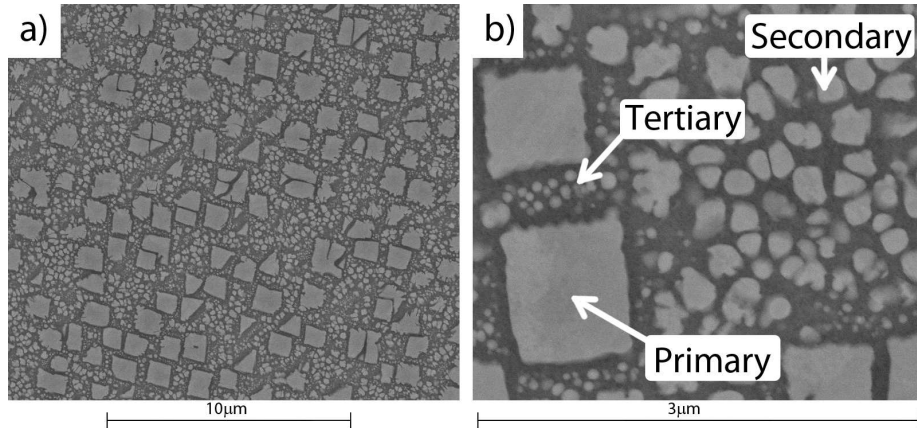
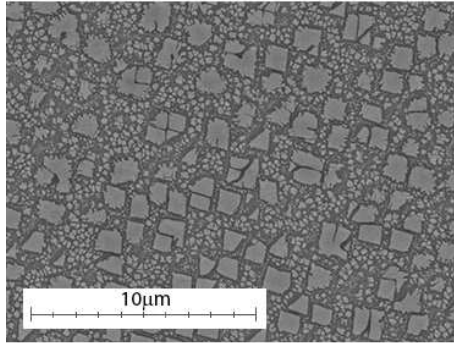


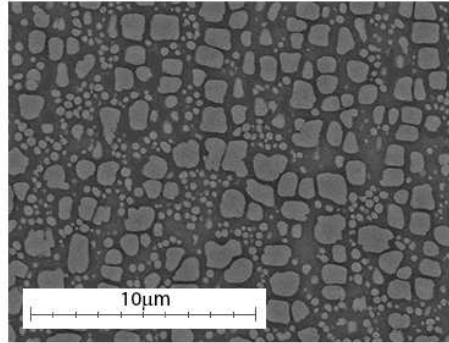
Figure 1: Scanning Electron Backscatter micrographs of IN738LC in the as-heat treated condition.

the temperatures 850°C and 900°C respectively. No secondary particles are observed after aging 10000 hours at 850°C. At 900°C a unimodal particle distribution is observed in the sample aged for 5000 hours. The morphology of the primary particles can be seen to evolve to a more globular form from the initial cuboidal geometry. Quantitative image analysis was performed using MATLAB image analysis toolbox. The accurate quantitative measurement of particle size from micrographs is challenging and prone to much error. Sources of error include over-etching and the image processing steps taken to identify individual particles. The total volume fraction of γ' in IN738 has been reported to be approximately 45% [24]. A higher value of 56% has also been measured by Smid *et al.* [25] with further confirmation from Strunz *et al.* [26]. The particle volume fraction may be estimated by the area fraction measured from micrographs [26, 27]. The measured area fraction of particles for the different conditions examined are presented in Table 2. The mean field modelling method used in this work assumes that the particles remain spherical during growth/dissolution. Measurements of the particle areas were performed from micrographs, and an equivalent radius was calculated by equating the measured particle area to that of a circle of equivalent area.

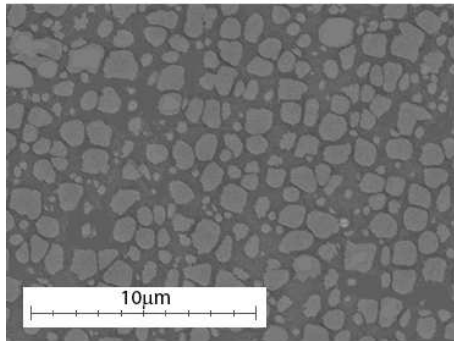
a) As recieved



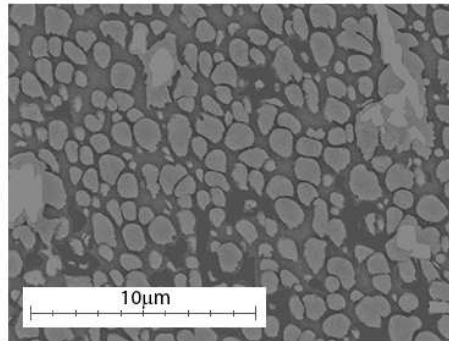
b) 1000h



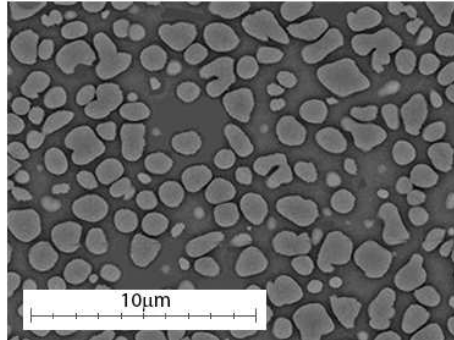
c) 2000h



d) 5000h



c) 2000h



d) 5000h

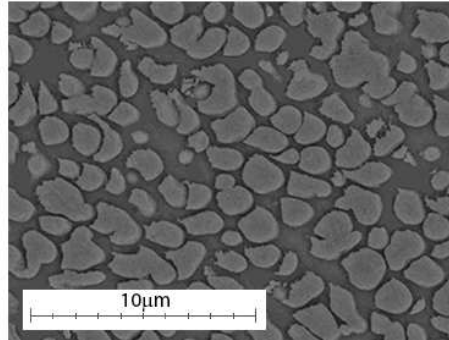
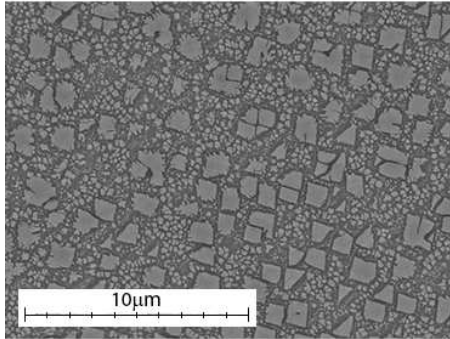
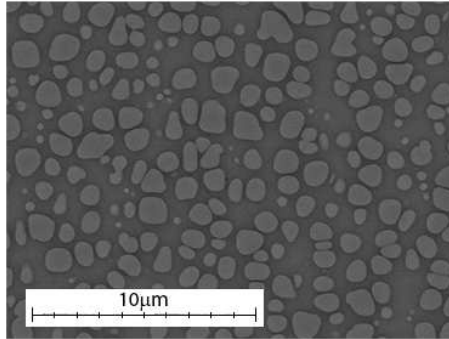


Figure 2: Scanning Electron Backscatter micrographs of IN738LC after different aging times at 850°C.

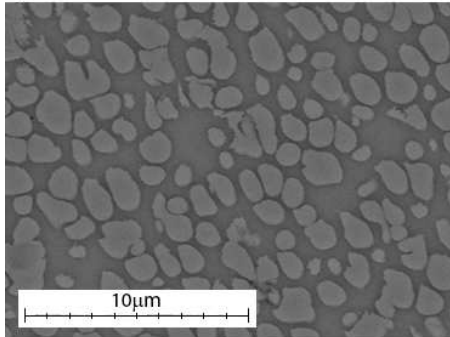
a) As recieved



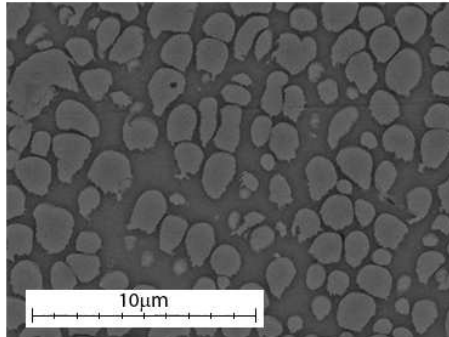
b) 1000h



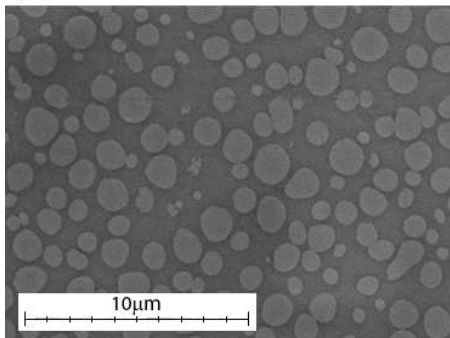
c) 2000h



d) 5000h



e) 2000h



f) 5000h

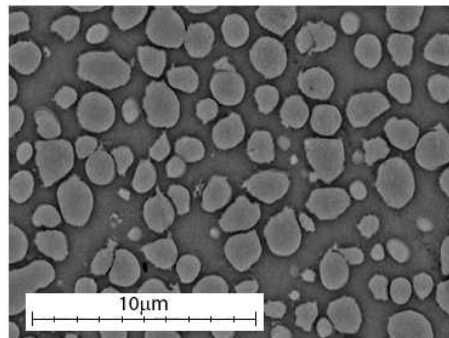


Figure 3: Scanning Electron Backscatter micrographs of IN738LC after different aging times at 900°C.

Condition	Area fraction
As received	45.0 ± 3.1
1000h at 850°C	47.4 ± 2.8
2000h at 850°C	59.3 ± 2.2
5000h at 850°C	51.3 ± 2.2
10000h at 850°C	46.6 ± 0.7
20000h at 850°C	54.3 ± 4.3
1000h at 900°C	41.8 ± 1.9
2000h at 900°C	47.9 ± 2.1
5000h at 900°C	51.2 ± 2.5
10000h at 900°C	38.5 ± 2.4
20000h at 900°C	49.5 ± 2.1

Table 2: The measured area fraction of particles (%)

For comparison between mean field prediction and experiment, it is necessary to approximate the three dimensional size of the particles observed in the micrographs. Such information is needed to determine the initial particle size distribution as an input for the mean field simulation. The method used follows that of Diogenes *et al.* [28]. The algorithm is illustrated in Figure 4. Gaussian waveforms are generated, approximating the three dimensional distribution of the particles. Particles are randomly sampled from this distribution. The sampled particles are then cut in a random position at a random orientation. The cross sectional area of the cut particle is then binned, and a distribution of cut sampled particles is generated. For convenience, the size of the particle is expressed in terms of the radius of a circle of equivalent area, even if the geometry is approximated by a cube opposed to a sphere. The generated distribution of 2D particle cross sections is then compared with the measured distribution from the micrographs. The parameters that create the Gaussian waveform descriptive of the three dimensional distribution are then calibrated until satisfactory agreement between measurement and prediction is achieved.

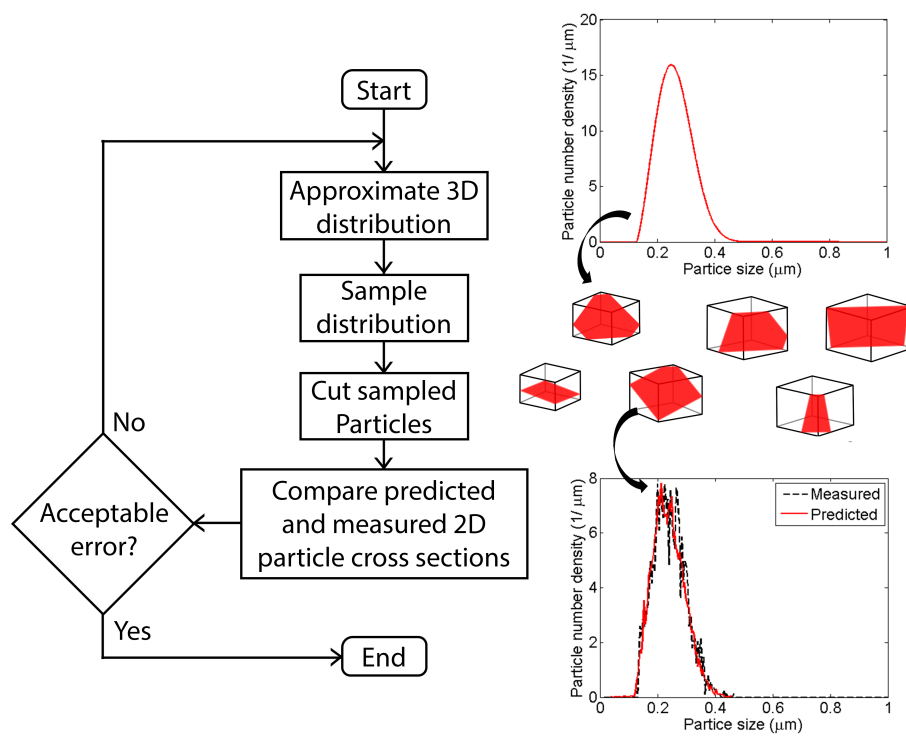


Figure 4: Method used to approximate the 3D size of precipitates.

In the as-received condition, the particles appear to be a combination of large cuboidal particles, and small globular particles. To approximate the three dimensional size of the particles within these microstructures, the large cuboidal particles are described by perfect cubes and the small globular particles by spheres. This approach assumes that the particles can be accurately separated by size and shape so that the cross sections of particles measured from the micrographs can be separated into either cuboidal or spherical particles. If the large primary particles are assumed to be cuboidal, and particle cross sections may be categorised as either spherical or cuboidal, it is then reasonable to approximate the volume fraction of spherical and cuboidal particles from the measured area fraction.

The particle size distribution is influenced by morphology. When considering a cuboidal geometry, the interception of a particle by a plane requires the specification of the cube orientation relative to the cutting plane. Furthermore, the plane can randomly intercept the particle at any location. Figure 5 shows the impact of different approximations on the 3D particle size distribution: (i) cuboidal with fixed orientation between the particle and cutting plane; (ii) cuboidal particles with random cutting orientation; and (iii) randomly cut spheres. Figure 5 (a) compares the measured and predicted accumulative probability whilst Figure 5 (b) presents the associated 3D particle size distributions. Best agreement was obtained when assuming the particle geometry as cubes which are cut in a fixed orientation. This is because the micrographs taken in this work cover too few grains and show little variation in the orientation of the cuboidal γ' precipitates. It can be seen that these assumptions regarding particle morphology have a significant impact upon the mean radius of the approximated 3D particle size distribution, with mean sizes varying between 430nm, 478nm and 523nm. The difference is as high as 9.4% when comparing distributions created from spherical geometry to those created from cubes with fixed cutting plane orientation.

This approach has been applied to all conditions examined. As the primary particles in the aged specimen appear more globular, they have been approx-

imated by spheres. The measured mean particle radius and corrected mean particle radius are given in table 3. The 3D approximations for the as-heat treated condition, the specimens aged at 850°C, and those aged at 900°C are shown in Figures 6, 11 and 12.

Condition	2D micrograph	3D approximation
1000h at 850°C	0.119 μm	0.150 μm
2000h at 850°C	0.286 μm	0.357 μm
5000h at 850°C	0.377 μm	0.468 μm
10000h at 850°C	0.465 μm	0.582 μm
20000h at 850°C	0.409 μm	0.506 μm
1000h at 900°C	0.348 μm	0.441 μm
2000h at 900°C	0.406 μm	0.508 μm
5000h at 900°C	0.501 μm	0.638 μm
10000h at 900°C	0.484 μm	0.593 μm
20000h at 900°C	0.607 μm	0.778 μm

Table 3: A comparison of the approximated 3D mean particle radius and the measurements taken from micrographs.

3. Mean Field Equations

Consider a random dispersion of γ' particles. Let the function $F(R, t)$ be the particle size distribution such that the number of particles per unit volume with radius between R and $R + dR$ at a time t is $F(R, t)dR$. The temporal evolution of $F(R, t)$ function is assumed to be governed by an advection partial differential equation with appropriate source term to account for the nucleation of particles:

$$\frac{\partial F(R, t)}{\partial t} + \frac{\partial F(R, t)V(R, t)}{\partial R} = I(R, t) \quad (1)$$

where $V(R, t)$ and $I(R, t)$ are the particle growth and nucleation rates, respectively. The particle concentration N_v , mean particle radius \bar{R} , and volume

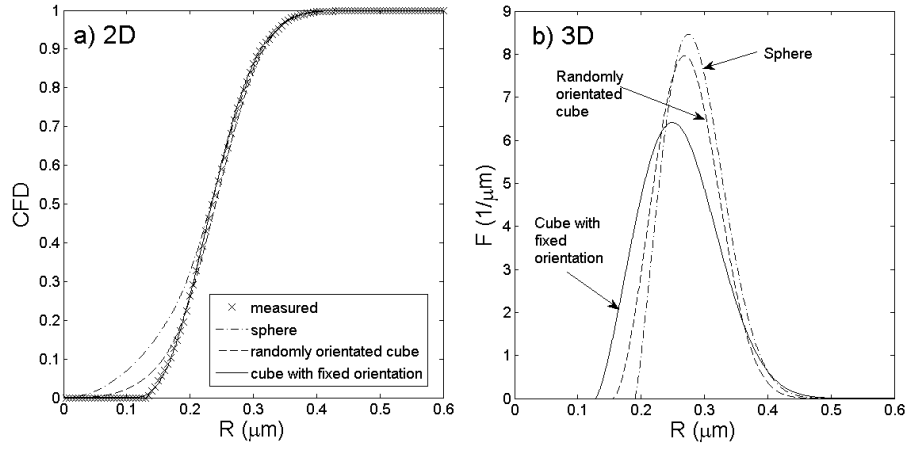


Figure 5: The impact of different approximations upon the calculated 3D particle size.

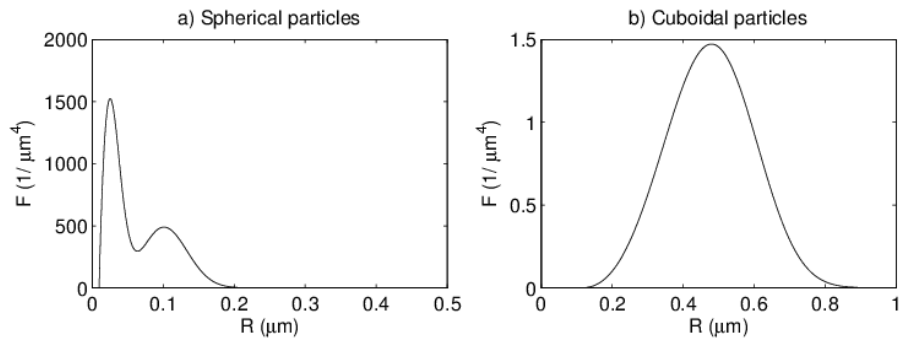


Figure 6: Approximated 3D particle size distribution for the as-heat treated condition.

fraction ϕ are determined by taking moments of $F(R, t)$ with respect to R ,

$$\begin{aligned} N_v &= \int_0^\infty F dR \\ \bar{R} &= \int_0^\infty RF dR / \int_0^\infty F dR \\ \phi &= \frac{4\pi}{3} \int_0^\infty R^3 F dR \end{aligned} \quad (2)$$

The particle growth rate has been shown to have the following form for spherical particles [29],

$$V(R, t) = \frac{A}{R(t)} \left(\frac{1}{R_c(t)} - \frac{1}{R(t)} \right) z \quad (3)$$

where the term A contains the effective diffusivity at the particle interface and R_c is the critical particle radius. Particles smaller than the critical particle radius shrink at the expense of particles larger than this value. In Equation (3), z is a factor that accounts for competitive growth of particles; $z = 1$ for non-competitive growth and $z \propto \phi^{1/2}$ for systems with a finite volume fraction [20]. Equation (3) was originally derived assuming interfacial energy and curvature driving diffusive flow to/away from a particle for a binary alloy. However, modern superalloys are characterised by complex chemistries that can include more than 10 components and misfit stresses associated with lattice parameter mismatch between the γ/γ' phases. These factors will modify the chemical potentials at the particle/matrix interface and therefore modify the particle growth rates. A number of workers have developed expressions for the particle interface velocity to include such details, however, at the expense of some simplifications. For example, the SFFK [18] approach used a volume expansion model to describe the misfit stress assuming isotropic elastic properties of the matrix and particle phases. However, the anisotropy of the elastic fields in real systems means that the misfit stresses will be rather more complex and will be a function of particle morphology and their spatial arrangement. Even so, the SFFK approach provides a good qualitative description of the key features influencing the particle growth rate and their model will be used in this study.

According to the SFFK the variables A and R_c take the following form,

$$A = \frac{2\sigma}{R_g T} \left[\sum_{i=1}^n \frac{(c_{ki} - c_{0i})^2}{c_{0i} D_{0i}} \right]^{-1} \quad (4)$$

$$R_c = \frac{2\sigma}{-\lambda - \sum_{i=1}^n c_{ki}(\mu_{ki} - \mu_{0i})} \quad (5)$$

where the interfacial energy is given by σ , the gas constant is given by R_g and the absolute temperature is given by T . If there are n alloying elements, the concentration of element i in the matrix and particle phase is given by c_{0i} and c_{ki} respectively. The chemical potentials with respect to element i in the matrix and particle phases is given by μ_{0i} and μ_{ki} . The diffusivity of element i in the matrix phase is given by D_{0i} . The term λ refers to the misfit strain energy and is approximated from Equation 6. The term ϵ_0 refers to the misfit strain, ν is Poisson's ratio and E is the elastic modulus.

$$\lambda = \frac{\epsilon_0^2 E}{1 - \nu} \quad (6)$$

The non-zero volume fraction correction factor for the SFFK model is given in Equation 7. For competitive growth Marqusee and Ross [20] showed how the particle growth rate is modified for a finite volume fraction dispersion of particles by the factor given by Equation 8. Svoboda and Fischer[18] have also derived an expression for z , given in Equation 9. The parameter k is a coefficient which Svoboda and Fischer approximated to have a value of 1.825 after calibrating steady state coarsening predictions to those of Voorhees and Glicksman [30]. This description of the z factor can only be applied to particles smaller than $kR_c/\phi^{1/3}$. This limitation becomes a problem during regimes of particle growth and coarsening, where the largest particle may be significantly larger than the critical particle radius. To apply Svoboda and Fischers z factor to the particle size distribution shown in Figure 6, the value of k was increased until numerical instability was avoided, reaching a value of 10.0.

$$z = 1 \quad \text{LSW} \quad (7)$$

$$z = 1 + R\sqrt{4\pi N_v \bar{R}} \quad \text{MR} \quad (8)$$

$$z = \left[1 - \left(\frac{R\phi^{1/3}}{kR_c} \right) \right]^{-1} \quad \text{SF} \quad (9)$$

It is not appropriate to apply analytical solutions of mean field models ($\bar{R}^3 - \bar{R}_0^3 = Kt$) to describe the coarsening kinetics of multi-modal particle size distributions. Such an approach cannot capture the transient evolution of the particle size distribution towards the asymptotic shape [5]. Once the particle size distribution has reached such a asymptotic shape, LSW mean field models predict a regime of steady state coarsening, suitable for the application of analytical models. A numerical implementation of a mean field model can capture the reduced growth kinetics of the mean particle size during this transient. The evolution of the particle size distribution may be determined through solving the continuity equation, given in Equation 1.

The continuity equation may be normalised to improve the accuracy of the calculation and decrease computation time. Spatial and temporal dimensions are normalised with respect to the variables R_k and τ , respectively, resulting in the normalised continuity Equation,

$$\frac{\partial f(r, t')}{\partial t'} + \frac{\partial f(r, t')v(r, t')}{\partial r} = q(r, t') \quad (10)$$

where

$$\begin{aligned} f(r, t')dr &\equiv F(R, t)R_k^3 dR \\ r &\equiv R/R_k \\ r_c &\equiv R_c/R_k \\ t' &\equiv t/\tau \\ \tau &\equiv \frac{R_k^3}{A} \end{aligned} \quad (11)$$

and the normalised source term for particle nucleation is given by q . The normalised moments are now given by Equation set 12, with the normalised particle

growth rate given in Equation 13.

$$\begin{aligned}
N_v &= \frac{1}{R_k^3} \int_0^\infty f dr = \frac{1}{R_k^3} n_v \\
\bar{R} &= \frac{R_k}{n_v} \int_0^\infty r f dr = R_k \bar{r} \\
\phi &= \frac{4\pi}{3} \int_0^\infty r^3 f dr
\end{aligned} \tag{12}$$

$$v = \frac{1}{r} \left(\frac{1}{r_c} - \frac{1}{r} \right) z \tag{13}$$

When modelling multi-modal distributions, the difference in particle number frequency density between primary and tertiary particles can result in loss of significance errors. This can be improved by describing the particle number frequency density by the volume occupied by particles. The normalised number frequency density, f of particles can be expressed in the terms of volume fraction frequency density, g . The volume fraction formulation space and reformulated continuity equation are given below:

$$\begin{aligned}
g(r, t') dr &\equiv \frac{4\pi}{3} f(r, t') r^3 dr \\
\frac{\partial g}{\partial t'} + \frac{\partial(gv)}{\partial r} &= \frac{3}{r} gv + \frac{4\pi r^3}{3} q
\end{aligned} \tag{14}$$

The reformulated moments are given in Equation set 15. The derivation of the reformulated continuity equation is given in the appendix.

$$\begin{aligned}
N_v &= \frac{3}{4\pi R_k^3} \int_0^\infty r^{-3} g dr \\
\bar{R} &= R_k \frac{\int_0^\infty r^{-2} g dr}{\int_0^\infty r^{-3} g} \\
\phi &= \int_0^\infty g dr
\end{aligned} \tag{15}$$

4. Numerical Implementation

A thermodynamic database may be used to calculate chemical potentials with a suitable mobility database for diffusivities. The TQ FORTRAN user interface in the commercial software ThermoCalc [31] has been used to calculate the chemical composition of γ' and the chemical potentials of the γ and γ' phases

for the alloy IN738LC . The thermodynamic database TTNi8 and mobility database MOBni1 were applied to the composition range given in table 2.

It is necessary to verify whether the available thermodynamic database is suitable for describing the alloy composition in interest. For IN738LC, there is considerable scatter reported in the literature regarding the γ and γ' phase diagram. As previously mentioned, the room temperature volume fraction of as-heat treated IN738LC should be in the region of 45% and 56% [24, 25]. Similar discrepancy exists with regard to the solvus temperature. Ojo *et al.* [32] observed dendritic segregation that caused different local γ' solvus temperatures. The Ti rich regions were found to have a solvus temperature of approximately 1180°C while the Al rich γ' prime particles had a solvus temperature of approximately 1120°C. Balikci *et al.* [27] suggest that the solutionising temperature is much higher at 1235°C, close to the solidus temperature measured by Chapman (1238°C) [33]. ThermoCalc with thermodynamic database TTNi8 predicts a lower solvus temperature, at 1140 C°C for the nominal composition of IN738LC, with a room temperature volume fraction of approximately 55%.

The impact of acceptable scatter within the alloy composition has been explored through assessing 10,000 different alloy compositions randomly sampled from the composition windows given in Table 2. The total weight percentage of Al and Ti was kept within the limits of 6.5% and 7.2%. Figure 7 (a) compares the predicted phase diagram with measurements reported from the literature and the area fractions made in this work. The boxplots show the variation in predicted behaviour considering acceptable scatter in alloy composition, with the solid line describing the predicted behaviour for the nominal composition. The range in predicted solvus temperatures is compared with published data in Figure 7 (b). The predicted solvus temperatures are within the scatter of reported solvus temperatures presented by Ojo *et al.* [32] and Balikci *et al.* [27].The predicted room temperature volume fraction of γ' is closer to the values reported by Smid *et al.*[25].

The element diffusivity was obtained from tracer diffusivities calculated using the MOBni1 mobility database. The lattice misfit, δ is given by $\delta =$

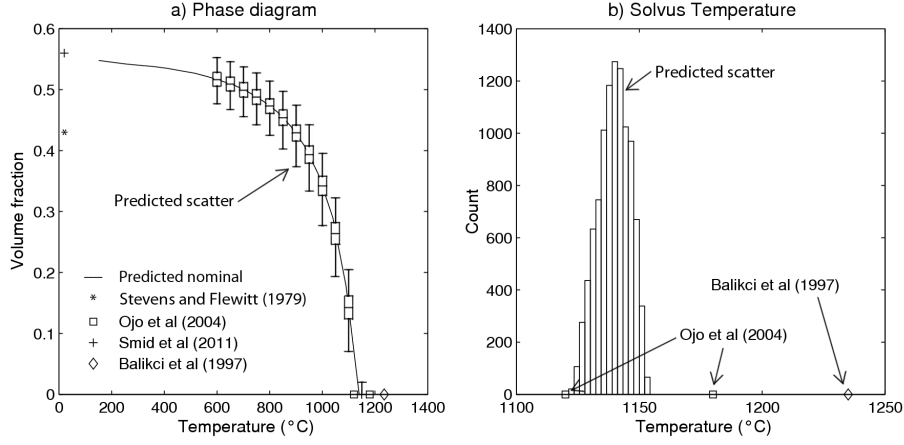


Figure 7: A comparison of the predicted γ' phase diagram with published data.

$2(a_{\gamma'} - a_{\gamma}) / (a_{\gamma'} + a_{\gamma})$. Li and Wahi [34] measured a lattice misfit strain varying between +0.04% and +0.08 %, with a proportionate relationship between the lattice misfit and the Aluminium content of the γ' particle. A value of 0.06% was used in the present calculations.

Mean field coarsening predictions are highly sensitive to the value used to define the interfacial energy, σ . The interfacial energy is a function of temperature and chemical composition [35, 36, 37, 38]. The interfacial energy may be approximated by fitting models to measured particle coarsening behaviour [39, 40], from thermodynamics [35], or from first principles [37]. Clouet *et al.* [41] describe a size dependence of the interfacial energy for small particles. Typical values descriptive of $Ni - Ni_3Al$ interfaces vary from 10 to 30 mJ/m^2 [37, 38, 40], with Olson *et al.* [42] reporting a value of 22.5 mJ/m^2 for the superalloy RR1000. The sensitivity of different model variants to the interfacial energy is presented in the results section. The model does not currently account for a particle size dependent interfacial energy and uses the same interfacial energy to describe the kinetics at 850 and 950 °C.

To decrease computation time, the following thermodynamic and mobility terms required from the SFFK model have been implemented using surrogate

models:

$$dG_C = \sum_{i=1}^n c_{ki}(\mu_{ki} - \mu_{0i}) \quad (16)$$

$$\theta \equiv \frac{AR_gT}{2\sigma} = \left[\sum_{i=1}^n \frac{(c_{ki} - c_{0i})^2}{c_{0i}D_{0i}} \right]^{-1} \quad (17)$$

The behaviour exhibited by these terms was most accurately captured by separating the kinetics into regimes of either growth, sub-solvus dissolution or super-solvus dissolution. The temperature was normalised by the solvus temperature such that $\Gamma = T/T_s$. The term φ was used to describe the normalised volume fraction, using Equation 18 or 19 for growth or dissolution regimes respectively.

$$\varphi_g = \phi/\phi_{eq} \quad (18)$$

$$\varphi_d = (\phi - \phi_{max})/(\phi_{max} - \phi_{eq}) \quad (19)$$

The term ϕ_{max} refers to the maximum volume fraction that may be obtained before an element is entirely partitioned to either the matrix or particle phase when assuming that the particle composition is at equilibrium. A look-up table was then used to interpolate the specific values of dG_C and θ for a given condition.

Different approaches to solving the continuity equation have been explored. The numerical method must be able to handle the divergence of the velocity field as the particle size approaches zero. The ability to use uneven grid spacing is desirable to allow the description of tertiary, secondary and primary particles with a reasonable number of elements. The fastest and most accurate scheme was found to be an explicit Hamilton-Jacobi ENO scheme, as described by Osher and Fedkiw [43]. The implementation by Baris Sumengen [44] was adapted to the purpose of describing mean field particle coarsening kinetics.

The method allows for a third-order accurate approximation of the spatial derivative from first-order accurate upwind differencing. Let the terms gv appearing in the spatial derivative of the continuity equation be described by ψ . The Hamilton-Jacobi ENO scheme described by Osher and Fedkiw is now out-

lined [43]. The second order accurate central differencing is described by $D_i^0\psi$:

$$D_i^0, \psi \approx \frac{\psi_{i+1} - \psi_{i-1}}{2\Delta r} \quad (20)$$

The first divided difference, $D_{i+1/2}^1, \psi$ is calculated from $D_i^0\psi$. The second divided difference, $D_i^2\psi$ is calculated from the first divided difference, and the third, $D_{i+1/2}^3\psi$ from the second:

$$\begin{aligned} D_{i+1/2}^1\psi &= \frac{D_{i+1}^0, \psi - D_i^0, \psi}{\Delta r} \\ D_i^2\psi &= \frac{D_{i+1/2}^1, \psi - D_{i-1/2}^1, \psi}{2\Delta r} \\ D_{i+1/2}^3\psi &= \frac{D_{i+1}^2, \psi - D_i^2, \psi}{3\Delta r} \end{aligned} \quad (21)$$

The spatial derivative is calculated using,

$$\frac{\partial\psi}{\partial r} = Q'_1 + Q'_2 + Q'_3 + O(h^3) \quad (22)$$

The coefficients Q'_1, Q'_2 , and Q'_3 , are determined from the first, second and third divided differences. The first coefficient is given by,

$$Q'_1(x_i) = D_{k+1/2}^1, \psi \quad (23)$$

where the value of the integer k is set to $i - 1$ or i for backward or forward differencing respectively. The second and third divided differences are calculated from the following Equations:

$$Q'_2(x_i) = c(2(i - k) - 1)\Delta r \quad (24)$$

$$Q'_3(x_i) = c^*(3(i - k^*)^2 - 6(i - k^*) + 2)(\Delta r)^2 \quad (25)$$

The value of c and k^* are dependent on the absolute magnitude of the second divided difference at the positions $D_k^2\psi$ and $D_{k+1}^2\psi$. If $|D_k^2\psi| \leq |D_{k+1}^2\psi|$, the value of k^* is set to $k - 1$ and c is set to $D_k^2\psi$. Otherwise, k^* is set to k and c is set to $D_{k+1}^2\psi$. The value of c^* depends upon the value of $|D_{k^*+1/2}^3\psi|$ compared with $|D_{k^*+3/2}^3\psi|$. If $|D_{k^*+1/2}^3\psi| \leq |D_{k^*+3/2}^3\psi|$, c^* equals $D_{k^*+1/2}^3\psi$, else the variable is equal to $D_{k^*+3/2}^3\psi$. A forward first order accurate finite difference is

then applied to the temporal derivative, obtaining the following solution to the continuity Equation:

$$g^{n+1} = g^n - (Q'_1 + Q'_2 + Q'_3)dt' + \frac{3}{r}gvd t' + \frac{4\pi r^3}{3}qdt' \quad (26)$$

The time step was controlled by a Courant-Friedrichs-Lewy condition, as shown below:

$$dt' = \min \left[\alpha \left(\frac{|v_i| + |q_i|}{\Delta r_i} \right)^{-1} \right] \quad (27)$$

The grid spacings that did not contain a significant number of particles were not included in the adaptive time step calculation.

5. Results

The mean field framework outlined in the previous two sections has been applied to model the particle coarsening behaviour of the nickel-based superalloy IN738LC during isothermal aging at the temperatures of 850 °C and 900 °C. Figure 6 shows the initial distribution required to solve the initial value problem defined in Section 3.

The following section details the sensitivity of the interfacial energy on particle size distribution evolution for different descriptions of multiple particle dispersions defined in section 3. The influence of competitive growth is assessed through the different z factors given in Equations 7,8 and 9. The subsequent sections present the model simulations of the particle size distributions evolution as a function of composition variation, and particle misfit strain energy.

5.1. The interfacial energy and the description of non-dilute particle systems.

The interfacial energy required to capture the experimental behaviour differs depending upon the z factor used to account for non-dilute particle dispersions. Numerical solutions have been obtained for the different expressions for the z factor given by Equations 7, 8, and 9 and will be referred to in this paper as the LSW (Lifshitz, Slyozov and Wagner), MR (Marqusee and Ross) and SF (Svoboda and Fischer) z factors, respectively

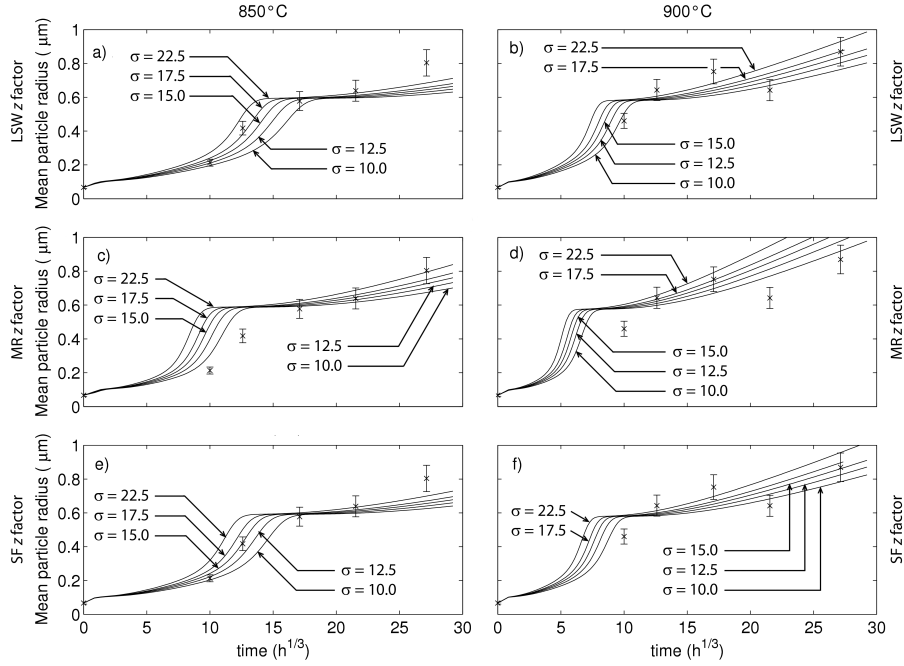


Figure 8: A comparison of predicted and measured mean particle radius, considering different interfacial energies (mJ/m^2) and z factors.

These calculations have used the nominal alloy composition. For the SF z factor, the value of k has been treated as a fitting parameter in the present analysis. Figure 8 compares the simulated particle coarsening behaviour, displaying the sensitivity of the interfacial energy upon calculations using the different z factors. The error bars in the mean particle size measurements include the error when approximating the 3D particle size. Figure 8 (a) and (b) describe the predictions using the LSW z factor for isothermal aging at 850°C and 900°C respectively. Similarly, Figure 8 (c) and (d), and ((e) and (f) present the predictions using the MR and SF z factors.

For both temperatures, it can be seen that all model predictions capture the plateau in mean particle radius (see Figures 8), similar to the behaviour observed by Coakley *et al.* [2]. The predictions are highly sensitive to the interfacial energy, impacting both the transition to a unimodal particle size

distribution and the shape of the unimodal particle size distribution. The LSW z factor requires a higher interfacial energy than the MR and SF z factors. The MR z factor accelerates particle growth significantly, and requires adjustment to the diffusivities obtained from DICTRA to capture the observed behaviour with greater accuracy.

Figures 9 and 10 show a comparison of the numerical solutions (using different z factor descriptions) and measured values for the mean particle radius, mean primary particle radius, the volume fraction of secondary particles and the total particle concentration at 850°C and 900°C, respectively. The error bars in the volume fraction measurements describe the error in measuring area fractions of particles from micrographs. The simulations have assumed an interfacial energy of 17.5 mJ/m² when using the LSW z factor and 15.0 mJ/m² when using the MR and SF z factors.

Figures 9 (b) and 10 (b) compare the measured and predicted mean primary particle radius. The predicted drop in mean primary particle size is due to the merging of the secondary and primary particles and the onset of the dissolution of primary particles. In Figures 9 (c) and 10 (c) the measured and predicted volume fractions of secondary particles are reasonable for 850°C; however, the mean field predictions overestimate the rate of dissolution at 900°C. Again, it can be seen that the MR factor predicts a significantly faster coarsening rate than the SF and LSW factors, over predicting the reduction in particle concentration, as shown in Figures 9 (d) and 10 (d).

Figures 11 and 12 compare the approximated 3D particle size probability densities obtained from micrographs to predictions for coarsening behaviour at 850°C and 900°C, respectively. The SF factor predicts most similar behaviour when considering the merging of the two distributions, however the shape of the unimodal distribution predicted by the MR distribution is flatter and closer to the experimentally measured unimodal particle size distributions as shown in Figure 13. Figure 13 compares the shape of predicted and measured particle size distributions for specimens aged for 20,000 hours at 900°C.

The finding that the MR z factor accelerates the rate of particle coarsening

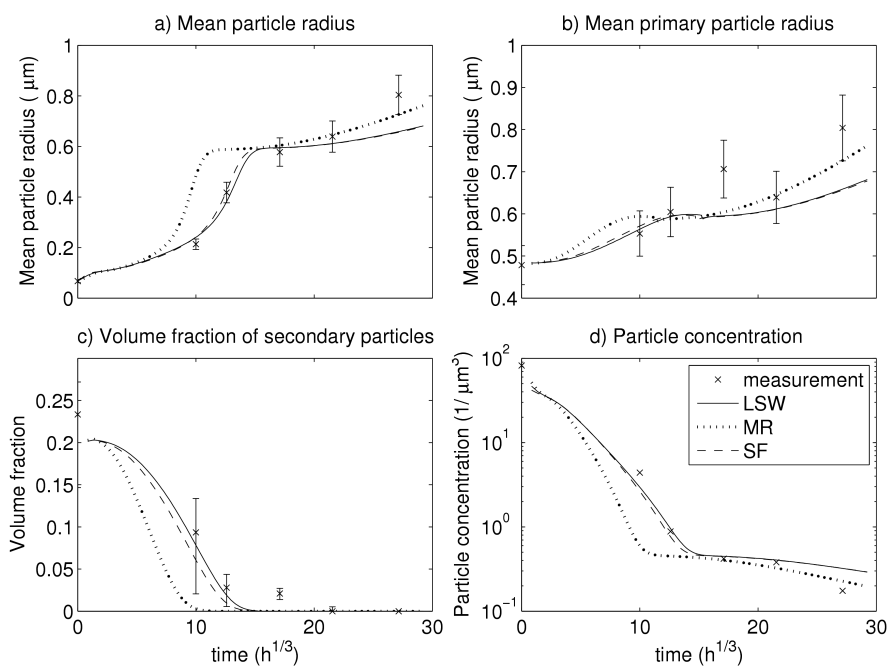


Figure 9: A comparison of predicted and measured statistical data during coarsening at 850°C .

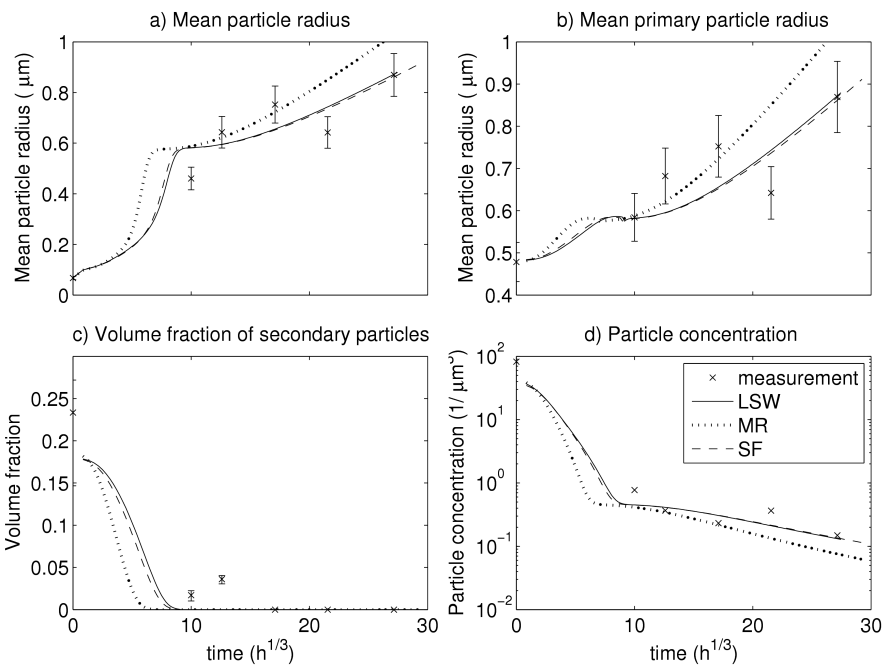


Figure 10: A comparison of predicted and measured statistical data during coarsening at 900°C.

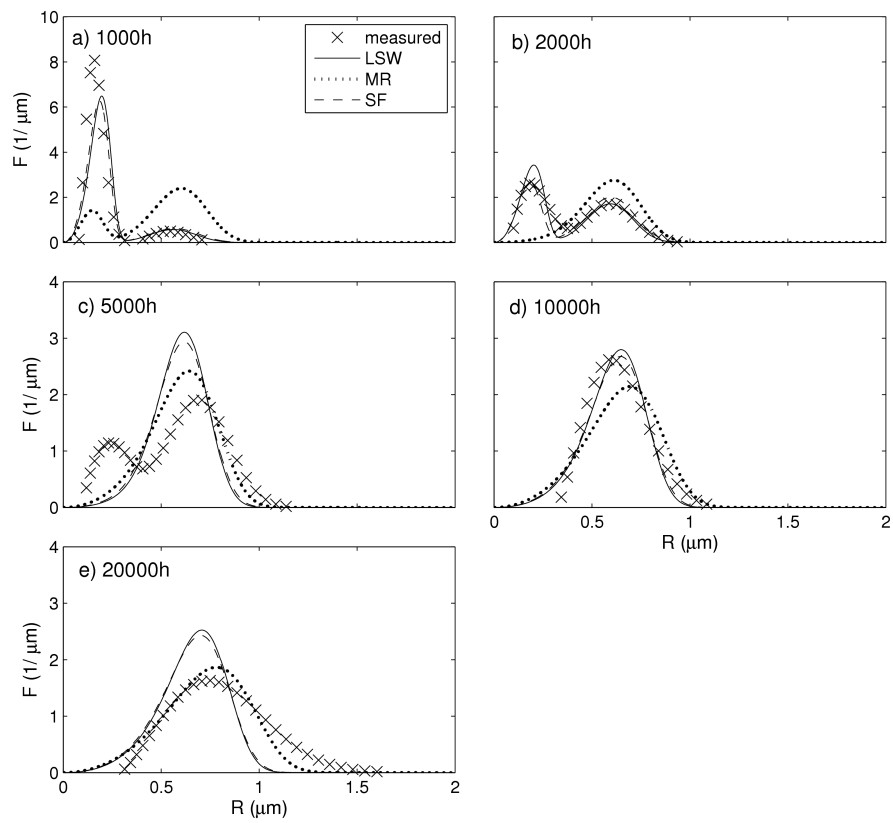


Figure 11: A comparison of the predicted and measured particle size distributions during aging at a temperature of 850°C .

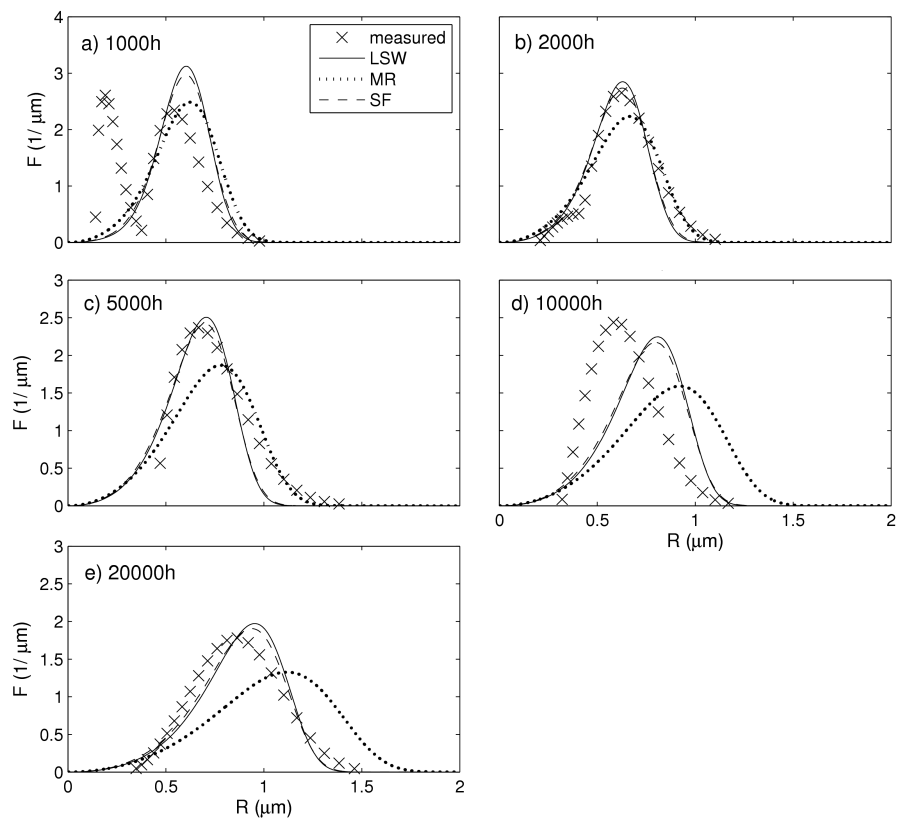


Figure 12: A comparison of the predicted and measured particle size distributions during aging at a temperature of 900°C .

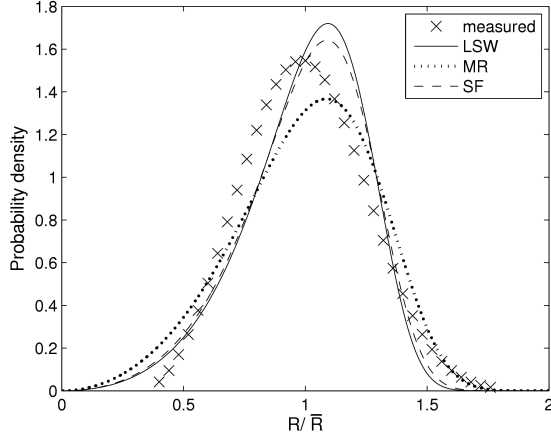


Figure 13: A comparison of the shape of predicted and measured distributions, after aging for 20,000 hours at 900°C .

compared to other descriptions is consistent with the findings of Wang *et al.* [45], when comparing the rate constant in the analytical solution of mean field models. Wang and Glicksman [46] offer an alternative z factor of similar form to the SF z factor, which however was found to be numerically unstable when applied to the initial particle size distribution.

5.2. The alloy composition.

It has been shown that the variations in composition within the alloy specification has a significant impact upon the predicted phase diagram (see Figure 7). Such variation in composition also influences chemical potentials and diffusivities and consequently the predicted coarsening behaviour. The impact of composition variation upon the thermodynamic and mobility parameters, dG_C and θ is shown in Figure 14 for two values of φ_g .

Changes in chemical composition have a larger impact upon dG_C and θ at lower temperatures and high values of φ_g . The impact of scatter in mobility and thermodynamic parameters affect the term A and critical particle radius shown in Equations 4 and 5 respectively.

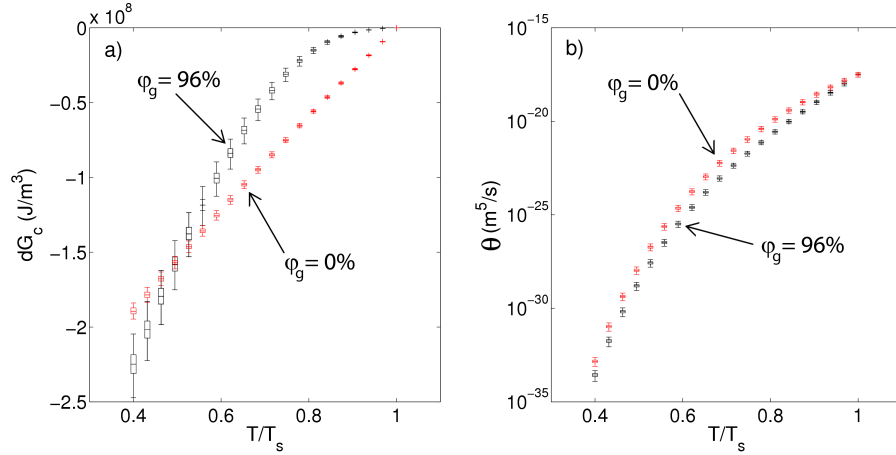


Figure 14: The predicted dG_C and θ as a function of normalised temperature considering acceptable variation in chemical composition

To determine the impact of variations in chemical composition upon the simulated particle coarsening kinetics, the isothermal aging simulation at 850° C has been repeated 200 times using bulk chemical compositions sampled from within the tolerance for IN738LC. Figure 15 compares the predictions to measurements, with Figures 15 (a), (b) and (c) comparing measurements to predictions for the mean particle radius, number concentration and total volume fraction of particles, respectively. Figure 15 (d) compares the predicted and measured particle size distributions after 20,000h at 850° C. Experimental measurements are presented by crosses with box plots describing the predictions as a result of scatter in chemical composition.

In Figures 15 (a) and (b) it can be seen that the scatter in predicted behaviour due to variation in chemical composition is largest during the transition from a bi-modal to a unimodal particle size distribution. Once the distribution reaches a unimodal particle size distribution, the predicted scatter in coarsening kinetics due to bulk composition variation is less than the experimental error.

Figure 15 (c) shows that the predicted scatter in volume fraction is large with $\pm 3.3\%$ of the mean prediction. This scatter is still less than that associated with measuring area fraction from micrographs, indicating that such behaviour

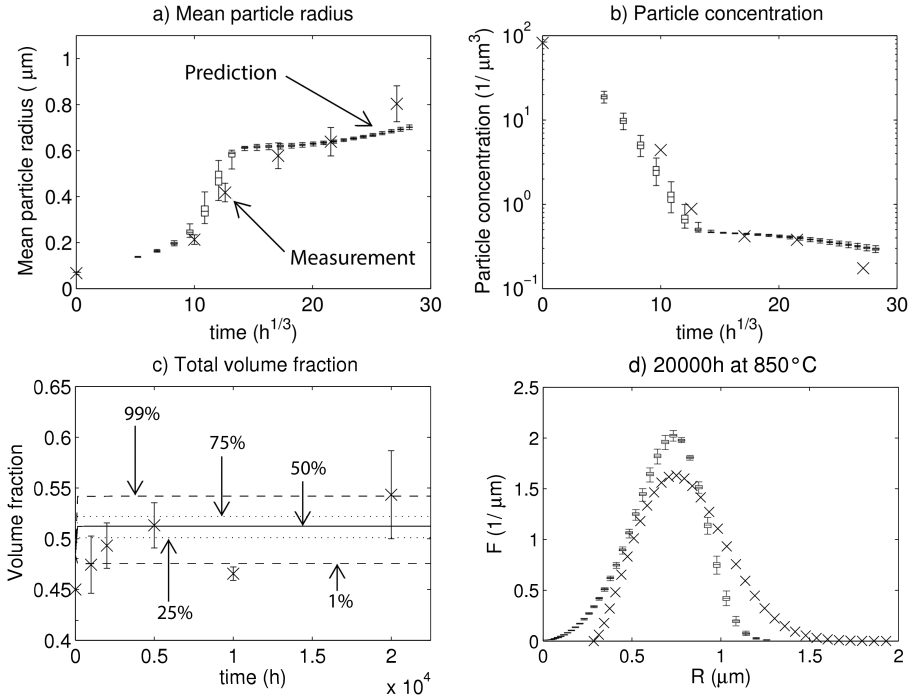


Figure 15: A comparison of predicted and measured behaviour during coarsening at 850°C considering variation in chemical composition.

is difficult to verify from this approach. The measured behaviour suggests that the volume fraction of particles may be increasing during coarsening, which is not currently captured by the model.

The fastest predicted coarsening kinetics are likely due to a combination of either a lower equilibrium volume fraction, faster mobilities or a larger critical particle radius than compared to the values calculated from the nominal composition. The scatter in predictions obtained in this section is descriptive of the variation in particle coarsening behaviour displayed by components originating from different batches of material.

The difference in local composition caused by the dendritic segregation of alloying elements as observed by Ojo *et al.* [32] cannot be treated in a similar manner as shown in this section as the degree of segregation would not remain

static during the heat treatment.

5.3. The misfit strain energy.

The influence of γ/γ' lattice misfit distortions on the γ' evolution has been studied by many authors [47, 48, 49, 50, 51]. It is known that the misfit strain energy has an important role in the morphological evolution of particles in nickel-based superalloys [48]. An example of such interactions is the phenomena of "inverse coarsening" as described by Su and Voorhees [49], where small particles may grow at the expense of larger particles. The behaviour was observed in a sharp-field interface model where energy minimisation included both interfacial and elastic strain energy. "Inverse coarsening" may explain why the model currently over predicts the rate of dissolution of the small secondary particles.

The framework developed by SFFK is able to account for lattice misfit strain energy. The misfit strain energy effects the critical particle radius through Equation 5. A sensitivity study has been performed, varying the lattice mismatch between 0.0% to 0.175%. As stated previously, the calculations assume the misfit strain energy to be isotropic and does not account for elastic interactions between neighbouring particles. The impact of the present model upon predicted isothermal coarsening at 850°C is shown in Figure 16. Figure 16 (a) and (b) compare the predicted mean particle radius to measurements with different values of lattice mismatch, δ . The model predicts a faster rate of dissolution of secondary particles when increasing the value of δ , however the long term aging behaviour is not significantly affected. This is observed when comparing the predicted and measured particle size distributions as shown in Figures 16(c) and (d) after 2000h and 10,000h respectively. The upper limit for δ from the measurements of Li and Wahi [34] describing un-deformed material does not have a significant effect upon the predicted behaviour.

The results indicate it is not possible to account for the inverse coarsening mechanism with the current formulation. To capture such behaviour it may be necessary to include the interaction strain between neighbouring particles.

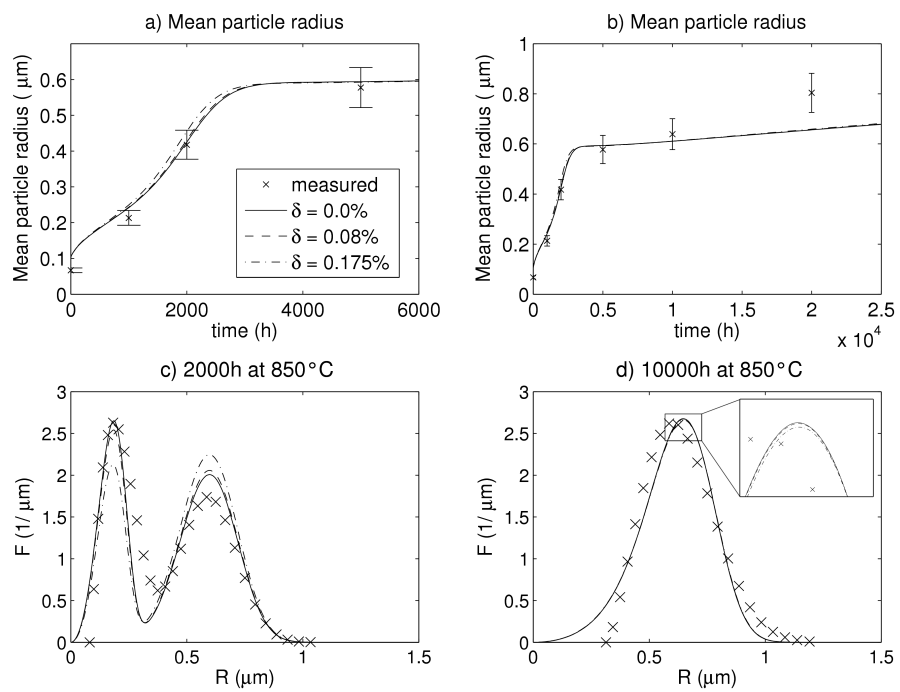


Figure 16: The impact of the lattice mismatch, δ upon the predicted particle coarsening at 850°C.

6. Discussion.

This work has applied a multi-component description of particle coarsening, investigating the impact of acceptable scatter in bulk composition upon the thermal stability of particle dispersions. It has been shown how the scatter in bulk composition affects the predicted particle coarsening kinetics through impacting the phase diagram, the thermodynamic variables and the mobility terms, as shown in Figures 7 a) and 14 b) and 14 c), respectively. The change in the phase diagram affects the volume fraction of particles, as shown in Figure 15 a), where the predicted volume fraction of particles varies by up to ± 3.3 %. Such change in volume fraction of particles must impact the mechanical properties of the precipitate strengthened material [52]. The ability to capture such details when calculating mechanical properties offers a powerful tool which may be applied to determine the relationship between the acceptable variation in chemical composition and component performance.

The results show that the predicted rate of particle coarsening is most sensitive to variation in bulk composition during the transient coarsening regime, as shown in Figure 15 a) and b). As many nickel based superalloys are heat treated to obtain multi-modal particle size distributions, the transient coarsening regime is very important with regards to component performance. The sensitivity of the transient coarsening kinetics to scatter in bulk composition is likely to contribute to the variation observed in mechanical properties between components originating from different batches of material.

When designing the chemical composition of a precipitate strengthened alloy, improved thermal stability of the particle phase may be obtained through consideration of the differences in thermodynamic and mobility parameters in addition to the phase diagram.

The simulated particle coarsening behaviour shows reasonable agreement with the measurements, despite many simplifying assumptions. The mean field model only describes Ostwald ripening behaviour, ignoring the impact of particle coalescence, morphological changes, and inverse coarsening. Evidence of particle

coalescence may be seen in the morphology of particles shown in Figures 1, 2 and 3.

The assumption of spherical particle geometry may impact the accuracy of predictions. The deviation of the particles from spherical geometry may cause inaccuracies in the calculated particle growth rates. Kozeschnik *et al.* [53] developed an approach for the inclusion of a shape factor within the particle growth rate descriptive of needle and disc shaped precipitates. A similar approach could describe the different kinetics of shapes changing from spheres to cubes. A more accurate description of particle shape may improve predictions; however the particle morphology changes observed in nickel-based superalloys are more complicated, with the formation of "ogdoadically diced cubes" [54].

The present mean field model implementation assumes that the particle composition is at equilibrium, similar to the approach of Radis *et al.* [16]. The errors incurred by this simplification may contribute to the differences in predicted behaviour. The chemical composition of γ' has been measured to vary between different size populations of particles with the smallest particles being furthest from predicted equilibrium compositions [55, 56]. The difference in local concentration gradient, diffusion kinetics and thermodynamic parameters between the secondary and primary particles would alter the predicted particle growth rate.

A number of micro-mechanisms are known to influence the high temperature mechanical behaviour of nickel based superalloys. These include the presence of misfit stresses resulting from lattice mismatch between the γ and γ' phases [48, 49, 47, 50, 51], dislocation shearing of the γ' [57], dislocations climbing over pinning γ' particles [52], the thermodynamic stability of the γ' particles [2, 1], cavitation [58, 59], and grain growth [60, 61]. The particle size, spacing and volume fraction have been shown to have a significant impact the creep and plastic response of precipitate strengthened alloys [62, 63, 64, 65]. For high volume fraction alloys the particle dispersion determines the mean free path, the rate-dependent behaviour at high temperatures (associated with climb of dislocation around particles), and the extent of stress transfer between the

matrix and particles by the volume fraction. In addition, the details of the dispersion (as well as loading conditions) will determine the operation of one or all of the following basic mechanisms: Orowan bowing, particle cutting, and dislocation climb [52].

The particle coarsening model presented in this work can be used to provide the input dispersion data for continuum description of deformation behaviour, such as Dysons model of creep [3]. Such an approach can account for a number of micro-mechanisms operating simultaneously, such as cavitation, internal stresses, particle coarsening, and dislocation multiplication. Basoalto *et. al.* [66] have applied this model to IN738LC to predict creep and fatigue behaviour. Basoalto *et. al.* [67] later presented a more detailed version of the model which links the particle dispersion to plastic deformation, including particle-matrix misfit stresses.

7. Conclusion

A multi-component mean field description of particle coarsening has been presented and applied to predict the particle coarsening behaviour of an engineering nickel based superalloy. The numerical implementation of the mean field model, including the multi-component SFFK [15] particle growth rate, has been applied to predict the isothermal coarsening kinetics of IN738LC. A suitable finite difference scheme has been presented, with a framework for the surrogate modelling of thermodynamic and mobility parameters.

The 3D conversion method of Diogenes *et al.* [28] has been applied to approximate the 3D particle size distributions of multi-modal particle dispersions. The assumptions regarding the morphology of cuboidal particles has a large impact upon both the shape and mean size of the approximated 3D particle size distribution. It has been shown that the difference in approximated mean size may be as high as 9% when considering whether to describe cuboidal particles as cubes opposed to spheres.

The model is successful in predicting slower growth kinetics of the mean

particle size in the transition from a multi-modal to unimodal particle size distribution when compared to the steady state solution of $t^{1/3}$.

Numerical investigation of the impact of variations in bulk composition upon particle coarsening has found to have a significant impact upon the volume fraction of particles, and the rate of particle coarsening during the transient coarsening regime, prior to the onset of steady state particle size distribution. This will result in variations in the transient particle size distribution and translate to scatter of observed mechanical properties.

When investigating different descriptions of the impact of the finite volume fraction on the particle size distribution evolution, it was found that the MR z factor increases the particle growth rate significantly compared to LSW kinetics. The SF z factor is an improvement upon LSW particle kinetics (see Figures 9 and 10); however is limited by the numerical stability of the k parameter.

The model currently over predicts the rate of dissolution of secondary particles. The reason for this difference may lie in the lack of the mechanisms of particle coalescence and "inverse coarsening" as described by Su et al [49]. The predicted long term coarsening kinetics was found to be insensitive to the misfit strain energy, using the approximation given by equation 6. To predict "inverse coarsening" within a mean field model, a more detailed description of the misfit strain energy is required.

Appendix: Volume fraction reformulation

The reformulation of the continuity equation in terms of a volume fraction particle frequency density, $g(r, t')$, will now be outlined. Using the definition of $g(r, t')$ given by Equation 14, its temporal derivative is given by:

$$\frac{\partial f}{\partial t'} = \frac{\partial}{\partial t'} \left(g \frac{3}{4\pi r^3} \right) = \frac{3}{4\pi r^3} \frac{\partial g}{\partial t'} \quad (28)$$

Similarly for the spatial derivatives,

$$\frac{\partial f v}{\partial r} = \frac{\partial}{\partial r} \left(g \frac{3}{4\pi r^3} v \right) \quad (29)$$

and applying the chain rule gives the following result:

$$\frac{\partial}{\partial r} \left(g \frac{3}{4\pi r^3} v \right) = \frac{3}{4\pi r^3} \left(\frac{\partial}{\partial r} (gv) - \frac{3}{r} gv \right) \quad (30)$$

The continuity equation now has an additional flux term, as shown in equation 31.

$$\frac{3}{4\pi r^3} \frac{\partial g}{\partial t'} + \frac{3}{4\pi r^3} \left(\frac{\partial}{\partial r} (gv) - \frac{3}{r} gv \right) = q \quad (31)$$

Acknowledgements

Both M.J.A and H.C.B would like to acknowledge RWE Npower and Rolls-Royce plc for funding this work. In addition, M.J.A and H.C.B. would like to thank Dr. Christos Argyrakis and Dr. Hang Wang for useful discussions during the course of the project. The computations described in this paper were performed using the University of Birmingham's BlueBEAR HPC service, which provides a High Performance Computing service to the University's research community. See <http://www.birmingham.ac.uk/bear> for more details.

References

- [1] R. Sharghi-Moshtaghin, S. Asgari, The influence of thermal exposure on the γ' precipitates characteristics and tensile behavior of superalloy in-738lc, *J. Mater. Process. Technol.* 147 (3) (2004) 343 – 350.
- [2] J. Coakley, H. Basoalto, D. Dye, Coarsening of a multimodal nickel-base superalloy, *Acta Mater.* 58 (11) (2010) 4019–4028.
- [3] B. Dyson, Use of CDM in materials modeling and component creep life prediction, *J. Press. Vess. Technol.* 122 (3) (2000) 281–296.
- [4] N. Zhou, D. C. Lv, H. L. Zhang, D. McAllister, F. Zhang, M. J. Mills, Y. Wang, Computer simulation of phase transformation and plastic deformation in IN718 superalloy: Microstructural evolution during precipitation, *Acta Mater.* 65 (2014) 270–286.

- [5] M. K. Chen, P. W. Voorhees, The dynamics of transient Ostwald Ripening, *Modell. Simul. Mater. Sci. Eng.* 1 (1993) 591–612.
- [6] G. Greenwood, The growth of dispersed precipitates in solutions, *Acta Metall.* 4 (3) (1956) 243 – 248.
- [7] I. M. Lifshitz, V. V. Slyozov, The kinetics of precipitation from supersaturated solid solutions, *J. Phys. Chem. Solids* 19 (1961) 35–50.
- [8] C. Z. Wagner, Theorie der alterung von niederschlagen durch umlonsen (Ostwald-reifung), *Z. Elektrochem* 65 (1961) 581–591.
- [9] X. Li, N. Saunders, A. Miodownik, The coarsening kinetics of γ' particles in nickel-based alloys, *Metall. Mater. Trans. A* 33 (11) (2002) 3367–3373.
- [10] C. J. Kuehmann, P. Voorhees, Ostwald ripening in ternary alloys, *Metall. Mater. Trans. A* 27 (1996) 937–943.
- [11] Z. G. Mao, C. Booth-Morrison, C. K. Sudbrack, G. Martin, D. N. Seidman, Kinetic pathways for phase separation: An atomic-scale study in Ni-Al-Cr alloys, *Acta Mater.* 60 (2012) 1871–1888.
- [12] H. Jou, P. Voorhees, G. Olson, Computer simulations for the prediction of microstructure/property variation in aeroturbine disks, in: Green, K.A *et. al.* (Ed.), *Superalloys 2004*, TMS Seven Springs Int Symp Comm; TMS High Temp Alloys Comm; ASM Int, 2004, pp. 877–886.
- [13] D. M. Collins, H. J. Stone, A modelling approach to yield strength optimisation in a nickel-base superalloy, *Int. J. Plast.* 54 (2014) 96–112.
- [14] T. Philippe, P. H. Voorhees, Ostwald ripening in multicomponent alloys, *Acta Mater.* 61 (11) (2013) 4239–4244.
- [15] J. Svoboda, F. D. Fischer, P. Fratzl, E. Kozeschnik, Modelling of kinetics in multi-component multi-phase systems with spherical precipitates - I: Theory, *Mater. Sci. Eng. A Struct. Mater.* 385 (1-2) (2004) 166–174.

- [16] R. Radis, M. Schaffer, M. Albu, G. Kothleitner, P. Poelt, E. Kozeschnik, Multimodal size distributions of γ' precipitates during continuous cooling of UDIMET 720 Li, *Acta Mater.* 57 (19) (2009) 5739–5747.
- [17] A. Baldan, Review Progress in Ostwald ripening theories and their applications to nickel-base superalloys - Part I: Ostwald ripening theories, *J. Mater. Sci.* 37 (11) (2002) 2171–2202.
- [18] J. Svoboda, F. D. Fischer, Generalization of the Lifshitz-Slyozov-Wagner coarsening theory to non-dilute multi-component systems, *Acta Mater.* 79 (2014) 304–314.
- [19] P. Voorhees, M. Glicksman, Solution to the multi-particle diffusion problem with applications to ostwald ripening - i. theory, *Acta Metall.* 32 (11) (1984) 2001 – 2011.
- [20] J. A. Marqusee, J. Ross, Theory of Ostwald Ripening Competitive growth and its dependence on volume fraction, *J. Chem. Phys.* 80 (1) (1984) 563–543.
- [21] C. Davies, P. Nash, R. Stevens, Effect of volume fraction of precipitate on Ostwald ripening, *Acta Metall. Mater.* 28 (2) (1980) 179–189.
- [22] K. Wang, M. Glicksman, Ostwald ripening in materials processing, in: J. Groza, J. Shackelford (Eds.), *Materials Processing Handbook*, CRC Press, 2007, Ch. 5, pp. 25–15–10.
- [23] E. J. Payton, P. J. Phillips, M. J. Mills, Semi-automated characterization of the γ' phase in Ni-based superalloys via high-resolution backscatter imaging, *Mater. Sci. Eng., A* 527 (10-11) (2010) 2684–2692.
- [24] R. A. Stevens, P. E. J. Flewitt, Effects of γ' precipitate coarsening during isothermal aging and creep of the nickel-base superalloy IN-738, *Mater. Sci. Eng.* 37 (3) (1979) 237–247.

- [25] M. Smid, M. Petrevec, J. Polak, K. Obrtlík, A. Chlupová, Analysis of the effective and internal cyclic stress components in the Inconel superalloy fatigued at elevated temperature, in: M. Heilmaier (Ed.), Euro Superalloys 2010, Trans Tech Publications Ltd, Stafa-Zurich, 2011.
- [26] P. Strunz, M. Petrevec, U. Gasser, J. Tobias, J. Polak, J. Saroun, Precipitate microstructure evolution in exposed IN738LC superalloy, *J. Alloys Compd.* 589 (2014) 462–471.
- [27] E. Balıkcı, A. Raman, R. A. Mirshams, Influence of various heat treatments on the microstructure of polycrystalline IN738LC, *Metall. Mater. Trans. A* 28 (1997) 1993–2003.
- [28] A. N. Diogenes, L. O. E. dos Santos, C. P. Fernandes, Particle size distribution correction method using a simulated annealing technique, *Therm Eng+* 10 (2011) 38–43.
- [29] R. Stevens, C. Davies, The unique attractor in the theory of Ostwald ripening, *Scripta Mater.* 46 (1) (2002) 19 – 23.
- [30] P. Voorhees, M. Glicksman, Solution to the multi-particle diffusion problem with applications to Ostwald ripening - ii. computer simulations, *Acta Metall.* 32 (11) (1984) 2013–2030.
- [31] J. Andersson, T. Helander, L. Haglund, P. F. Shi, B. Sundman, THERMOCALC & DICTRA, computational tools for materials science, *CALPHAD* 26 (2) (2002) 273–312.
- [32] O. A. Ojo, R. L. Richards, M. C. Chaturvedi, On incipient melting during high temperature heat treatment of cast Inconel 738 superalloy, *Mater. Sci. Eng* 39 (24) (2004) 7401–7404.
- [33] L. Chapman, Application of high temperature DSC technique to nickel based superalloys, *J. Mater. Sci.* 39 (24) (2004) 7229–7236.

- [34] J. Li, R. Wahi, Investigation of γ/γ' lattice mismatch in the polycrystalline nickel-base superalloy IN738LC: Influence of heat treatment and creep deformation, *Acta Metall.* 43 (2) (1995) 507–517.
- [35] G. Kaptay, On the interfacial energy of coherent interfaces, *Acta Mater.* 60 (19) (2012) 6804–6813.
- [36] E. Clouet, M. Nastar, C. Sigli, Nucleation of Al_3Zr and Al_3Sc in aluminum alloys: From kinetic Monte Carlo simulations to classical theory, *Phys. Rev. B: Condens. Matter* 69 (6).
- [37] C. Woodward, A. van de Walle, M. Asta, D. R. Trinkle, First-principles study of interfacial boundaries in Ni-Ni₃Al, *Acta Mater.* 75 (2014) 60–70.
- [38] A. Baldan, Review Progress in Ostwald ripening theories and their applications to the γ' -precipitates in nickel-base superalloys - Part II - Nickel-base superalloys, *J. Mater. Sci.* 37 (12) (2002) 2379–2405.
- [39] H. Calderon, P. Voorhees, J. Murray, G. Kostorz, Ostwald ripening in concentrated alloys, *Acta Metall.* 42 (3) (1994) 991–1000.
- [40] A. J. Ardell, Al-L_{12} interfacial free energies from data on coarsening in five binary Ni alloys, informed by thermodynamic phase diagram assessments, *J. Mater. Sci.* 46 (14) (2011) 4832–4849.
- [41] E. Clouet, A. Barbu, L. Lae, G. Martin, Precipitation kinetics of Al_3Zr and Al_3Sc in aluminum alloys modeled with cluster dynamics, *Acta Mater.* 53 (8) (2005) 2313–2325.
- [42] G. B. Olson, H. J. Jou, J. Jung, J. T. Sebastian, A. Misra, I. Locci, D. Hull, Precipitation model validation in 3(rd) generation aeroturbine disc alloys, in: Reed, RC *et. al.* (Ed.), *Superalloys 2008*, 2008, pp. 923–932.
- [43] S. Osher, R. Fedkiw, Level set methods and dynamic implicit surfaces, Springer-Verlag New York Inc., New York, USA, 2002.

- [44] B. Sumengen, A matlab toolbox implementing level set methods@ONLINE (2005).
URL <http://barissumengen.com/>
- [45] K. Wang, M. Glicksman, K. Rajan, Length scales in phase coarsening: Theory, simulation, and experiment, *Comput. Mater. Sci.* 34 (3) (2005) 235–253.
- [46] K. G. Wang, M. E. Glicksman, Phase Coarsening in Thin Films, *JOM* 67 (8) (2015) 1905–1912.
- [47] M. Thompson, C. Su, P. Voorhees, The equilibrium shape of a misfitting precipitate, *Acta Metall.* 42 (6) (1994) 2107–2122.
- [48] M. Doi, Coarsening behaviour of coherent precipitates in elastically constrained systems, *Mater. Trans., JIM* 33 (7) (1992) 637–649.
- [49] C. Su, P. Voorhees, The dynamics of precipitate evolution in elastically stressed solids - i. inverse coarsening, *Acta Mater.* 44 (5) (1996) 1987 – 1999.
- [50] X. Zhao, R. Duddu, S. P. A. Bordas, J. Qu, Effects of elastic strain energy and interfacial stress on the equilibrium morphology of misfit particles in heterogeneous solids, *J. Mech. Phys. Solids* 61 (6) (2013) 1433–1445.
- [51] K. Thornton, N. Akaiwa, P. Voorhees, Large-scale simulations of Ostwald ripening in elastically stressed solids: I. Development of microstructure, *Acta Mater.* 52 (5) (2004) 1353–1364.
- [52] L. Brown, R. Ham, *Strengthening Methods in Crystals*, Elsevier, Amsterdam, 1971.
- [53] E. Kozeschnik, J. Svoboda, F. D. Fischer, Shape factors in modeling of precipitation, *Mater. Sci. Eng., A* 441 (1-2) (2006) 68–72.
- [54] R. Rosenthal, D. R. F. West, Continuous γ' precipitation in directionally solidified IN738 LC alloy, *Mater. Sci. Technol.* 15 (1999) 1387–1394.

- [55] A. R. P. Singh, S. Nag, S. Chattopadhyay, Y. Ren, J. Tiley, G. Viswanathan, H. L. Fraser, R. Banerjee, Mechanisms related to different generations of γ' precipitation during continuous cooling of a nickel base superalloy, *Acta Mater.* 61 (1) (2013) 280–293.
- [56] Y. Q. Chen, T. J. A. Slater, E. A. Lewis, E. M. Francis, M. G. Burke, M. Preuss, S. J. Haigh, Measurement of size-dependent composition variations for gamma prime (γ') precipitates in an advanced nickel-based superalloy, *Ultramicroscopy* 144 (2014) 1–8.
- [57] A. Takahashi, M. Kawanabe, N. M. Ghoniem, γ' -precipitate strengthening in nickel-based superalloys, *Philos. Mag.* 90 (27-28) (2010) 3767–3786.
- [58] B. F. Dyson, M. S. Loveday, M. J. Rodgers, Grain boundary cavitation under various states of applied stress, *P. Roy. Soc. Lond. A Mat.* 349 (1657) (1976) 245–259.
- [59] M. Kassner, T. Hayes, Creep cavitation in metals, *Int. J. Plasticity* 19 (10) (2003) 1715 – 1748.
- [60] D. M. Collins, B. D. Conduit, H. J. Stone, M. C. Hardy, G. J. Conduit, R. J. Mitchell, Grain growth behaviour during near- γ' solvus thermal exposures in a polycrystalline nickel-base superalloy, *Acta Mater.* 61 (9) (2013) 3378–3391.
- [61] E. J. Payton, G. Wang, M. J. Mills, Y. Wang, Effect of initial grain size on grain coarsening in the presence of an unstable population of pinning particles, *Acta Mater.* 61 (4) (2013) 1316–1326.
- [62] R. Stevens, P. Flewitt, The dependence of creep rate on microstructure in a γ' -strengthened super-alloy, *Acta Metall. Mater.* 29 (5) (1981) 867–882.
- [63] M. Preuss, J. Q. da Fonseca, B. Grant, E. Knoche, R. Moat, M. Daymond, The effect of γ' particle size on the deformation mechanism in an advanced polycrystalline nickel-base superalloy, in: Reed, RC *et. al.* (Ed.), *SUPERALLOYS 2008*, 2008, pp. 405–414.

- [64] B. Reppich, Some new aspects concerning particle hardening mechanisms in γ' precipitating Ni-base alloys .1. Theoretical concept, *Acta Metall. Mater.* 30 (1) (1982) 87–94.
- [65] B. Dyson, M. McLean, Particle-coarsening, Sigma-0 and tertiary creep, *Acta Metall. Mater.* 31 (1) (1983) 17–27.
- [66] H. Basoalto, B. Dyson, M. McLean, A quantitative physics-based approach to creep and LCF life prediction: Application to nickel-base superalloys, in: Fuchs, G *et. al.* (Ed.), *Advanced materials and processes for gas turbines*, 2003, pp. 53–61.
- [67] H. C. Basoalto, J. W. Brooks, I. Di Martino, Multiscale microstructure modelling for nickel based superalloys, *Mater. Sci. Tech. Ser.* 25 (2) (2009) 221–227.